

# Bottom-up control of geomagnetic secular variation by the Earth's inner core

Julien Aubert<sup>1</sup>, Christopher C. Finlay<sup>2</sup> & Alexandre Fournier<sup>3</sup>

Temporal changes in the Earth's magnetic field, known as geomagnetic secular variation, occur most prominently at low latitudes in the Atlantic hemisphere<sup>1,2</sup> (that is, from  $-90$  degrees east to  $90$  degrees east), whereas in the Pacific hemisphere there is comparatively little activity. This is a consequence of the geographical localization of intense, westward drifting, equatorial magnetic flux patches at the core surface<sup>3</sup>. Despite successes in explaining the morphology of the geomagnetic field<sup>4</sup>, numerical models of the geodynamo have so far failed to account systematically for this striking pattern of geomagnetic secular variation. Here we show that it can be reproduced provided that two mechanisms relying on the inner core are jointly considered. First, gravitational coupling<sup>5</sup> aligns the inner core with the mantle, forcing the flow of liquid metal in the outer core into a giant, westward drifting, sheet-like gyre<sup>6</sup>. The resulting shear concentrates azimuthal magnetic flux at low latitudes close to the core–mantle boundary, where it is expelled by core convection and subsequently transported westward. Second, differential inner-core growth<sup>7,8</sup>, fastest below Indonesia<sup>6,9</sup>, causes an asymmetric buoyancy release in the outer core which in turn distorts the gyre, forcing it to become eccentric, in agreement with recent core flow inversions<sup>6,10,11</sup>. This bottom-up heterogeneous driving of core convection dominates top-down driving from mantle thermal heterogeneities, and localizes magnetic variations in a longitudinal sector centred beneath the Atlantic, where the eccentric gyre reaches the core surface. To match the observed pattern of geomagnetic secular variation, the solid material forming the inner core must now be in a state of differential growth rather than one of growth and melting induced by convective translation<sup>7,8</sup>.

The peculiar geographical localization (both in latitude and longitude, Fig. 1a and b, respectively) of geomagnetic secular variation observed during the historical era<sup>1</sup> (AD 1590–1990) has now been mapped to an unprecedented level of accuracy by virtue of more than one decade of global and continuous satellite magnetic observations. Recent models<sup>12–14</sup> benefit from improved removal of the contribution from external fields, and are now reliably able to resolve structures down to a 1,500-km lateral extent at the Earth's core–mantle boundary (spherical harmonic degree 13, Fig. 2a, b). To exploit this wealth of data fully, and uncover the dynamical processes operating in the Earth's core, it is necessary to combine magnetic observations with numerical models of the geodynamo<sup>15</sup>. These have steadily improved over the past two decades, with the standard models now well understood, thanks to concerted benchmarking activities and systematic exploration of the accessible parameter space<sup>16</sup>. Despite this progress, success in understanding the geomagnetic secular variation and predicting its future evolution remains conditional on our ability to explain its detailed structure with physical mechanisms simple and robust enough to withstand extrapolation from the simplified working regime of current models to the conditions of Earth's core. An outstanding difficulty for standard models has been how to reproduce the westward drift of low-latitude magnetic flux patches at the core–mantle boundary<sup>3,14</sup> in a self-consistent fashion. Quasi-steady westward drift has

previously been obtained<sup>17–19</sup>, but it becomes erratic<sup>16</sup> in models where magnetic field advection becomes realistically strong relative to diffusion. Furthermore, the Atlantic–Pacific asymmetry in the kinematics of these patches suggests some form of heterogeneous boundary control<sup>6</sup>. The combined effect on secular variation of top-down forcing from lower-mantle thermal anomalies<sup>20</sup> versus bottom-up forcing from the recently discovered inner-core translational instability<sup>7,8</sup> has remained unexplored.

Our coupled Earth numerical dynamo model (Methods) addresses these issues by building on the well understood basis of standard geodynamo models<sup>16</sup> and including some simple ingredients from early

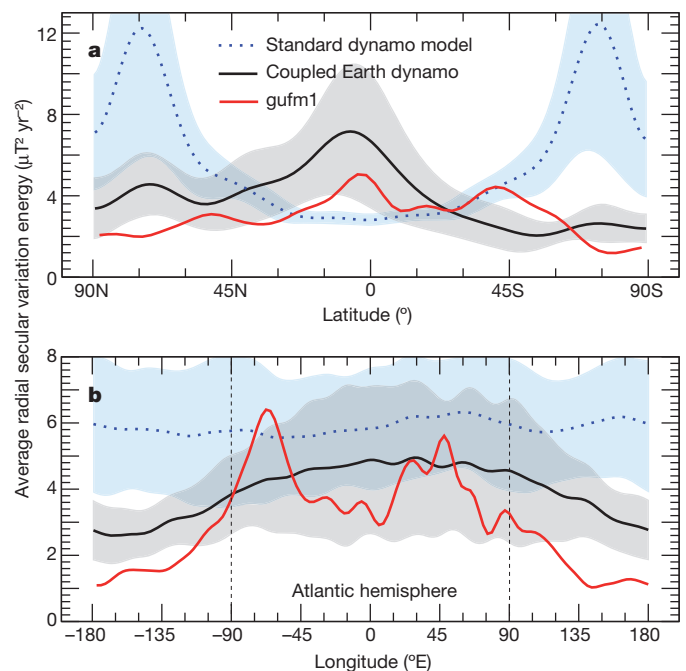


**Figure 1 | Geographical localization of geomagnetic secular variation.** **a, b**, Profiles of the time-averaged radial secular variation energy, averaged over longitude (**a**) or latitude (**b**). In each panel, data are taken from the historical geomagnetic field model<sup>1</sup> gufm1 (red line; spanning AD 1590–1990 and evaluated at the core–mantle boundary), from 400-year time-averages successively taken within a 83,000-year sequence of a standard numerical dynamo model (dotted blue line, average profile; blue shading,  $\pm 1$  s.d. in the distribution of 400-year time averages), and within a 67,000-year sequence of our coupled Earth dynamo model (black line, average profile; grey shading,  $\pm 1$  s.d. in the distribution of 400-year time averages). The numerical dynamo outputs are filtered at spherical harmonic degree and order 8, and the gufm1 model is presented at native resolution. The standard model has rigid, electrically insulating and non-moving boundaries. The coupled Earth dynamo model includes visco-magnetic outer-core/inner-core coupling, gravitational inner-core/mantle coupling, and thermochemical, heterogeneous coupling between the outer core, inner core and mantle.

<sup>1</sup>Dynamique des Fluides Géologiques, Institut de Physique du Globe de Paris, Sorbonne Paris Cité, Université Paris Diderot, UMR 7154 CNRS, F-75005 Paris, France. <sup>2</sup>Division of Geomagnetism, National Space Institute, Technical University of Denmark, Elektrovej, 2800 Kongens Lyngby, Denmark. <sup>3</sup>Géomagnétisme, Institut de Physique du Globe de Paris, Sorbonne Paris Cité, Université Paris Diderot, UMR 7154 CNRS, F-75005 Paris, France.

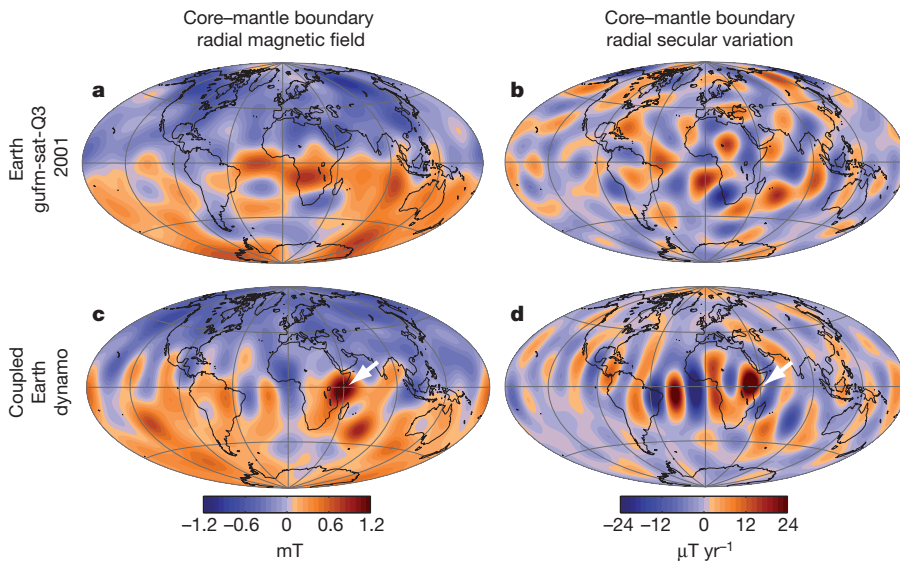


**Figure 2 | Maps of the magnetic field and secular variation.** a–d, Atlantic-centred Hammer projections of the core–mantle boundary radial magnetic field (a, c) and its temporal rate of change or radial secular variation (b, d); data are from geomagnetic field model<sup>14</sup> gufm-sat-Q3 in 2001 (a, b) and a snapshot of the coupled Earth dynamo model (c, d; orange denotes an outward magnetic field), both filtered at spherical harmonic degree and order 13. White arrows in c and d mark a location chosen for further analysis in Figs 3 and 4.

modelling efforts<sup>17,21,22</sup> that have recently been neglected. A field morphology similar to that of the Earth<sup>4</sup> (Fig. 2 and Extended Data Fig. 1) is achieved by choosing ratios of the timescales for magnetic induction, magnetic diffusion and the length of the day as close as computationally feasible to their Earth counterparts. We compromise on the ratio of the length of the day to the viscous diffusion timescale (the Ekman number,  $Ek$ ), which, although low, lies an order of magnitude above

state-of-the-art values<sup>18,19</sup>, in order to facilitate a parameter space exploration (Supplementary Information and Extended Data Table 1). The influence of viscosity is further mitigated by adopting a stress-free mechanical condition at the core–mantle boundary.

Robust westward drift and time-dependence of low-latitude secular variation similar to that observed over the past 400 years are achieved in the coupled Earth dynamo model through a mechanism based on indirect exchanges of angular momentum between the outer core and the mantle via the inner core. The inner core couples with the outer core primarily through a magnetic torque, which dominates at the Ekman number studied. At the base of the outer core, thermochemical ‘winds’ resulting from the interaction of the Coriolis force with convective upwellings entrain the inner core in the eastward direction<sup>21,23</sup> with respect to the planetary rotating frame. But a gravitational torque<sup>5,22–24</sup>, resulting from coupling between lower-mantle mass anomalies and the induced topography at the inner-core surface, transfers angular momentum between the inner core and mantle. In a situation where it only experiences this gravitational torque, the mantle is then also entrained in the eastward direction. Conservation of angular momentum in the planetary rotating frame then requires a sustained westward flow (see below) with respect to the mantle in the uppermost part of the outer core<sup>6,22</sup>. Both the gravitational torque and the net torque exerted by the outer core on the inner core vanish when averaged over time (Methods). This leads to long-term co-rotation between the mantle, inner core and lower outer core, with thermochemical wind gradients maintaining the westward drift in the upper outer core. For a given convective forcing, this drift is maximized if direct coupling between the outer core and the mantle is much weaker than indirect coupling via the inner core, as is the case in the coupled Earth dynamo model.

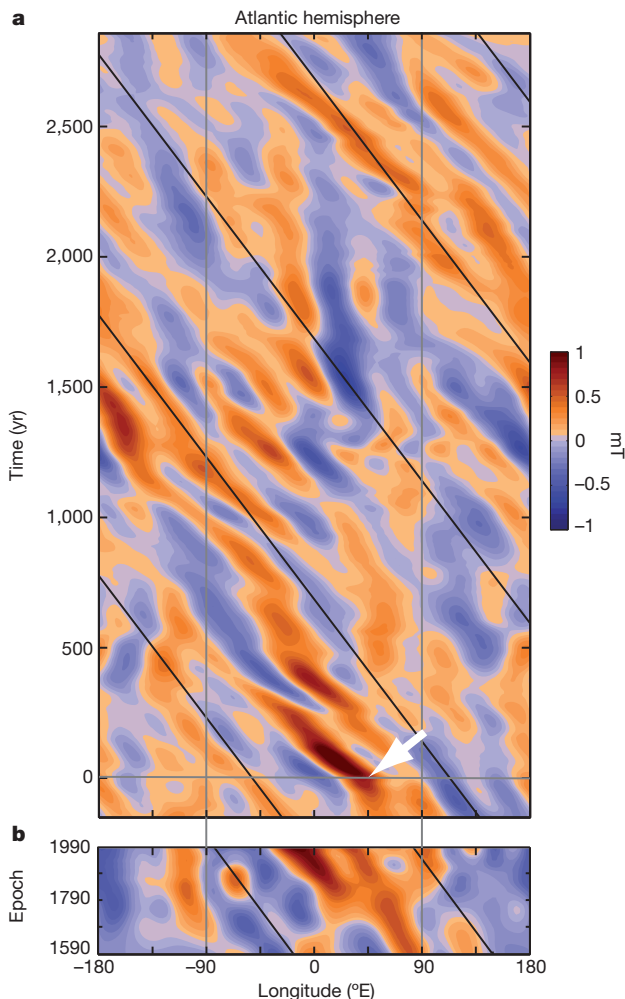


**Figure 3 | Temporal evolution of magnetic structures at the Equator.**

a, b, Time–longitude plot of the radial magnetic field at the Equator evaluated at the core–mantle boundary (orange denotes an outward magnetic field) from a 3,000-year sequence of the coupled Earth dynamo model filtered to spherical harmonic degree and order 8 (a), and from the 400-year sequence of geomagnetic field model<sup>1</sup> gufm1 at its native resolution (b). Grey vertical lines mark the Atlantic hemisphere. The grey horizontal line (model time 0) marks the time of the snapshot presented in Figs 2 and 4, and the white arrow marks the reference location. The model time 0 is chosen to be the start of a magnetic patch emergence and drift sequence representative of the localization of secular variation diagnosed in Fig. 1. See Supplementary Video for the evolution of magnetic features at all latitudes in the coupled Earth dynamo model over the entire temporal sequence. The slanted black lines denote a reference westward drift velocity of  $10 \text{ km yr}^{-1}$ .

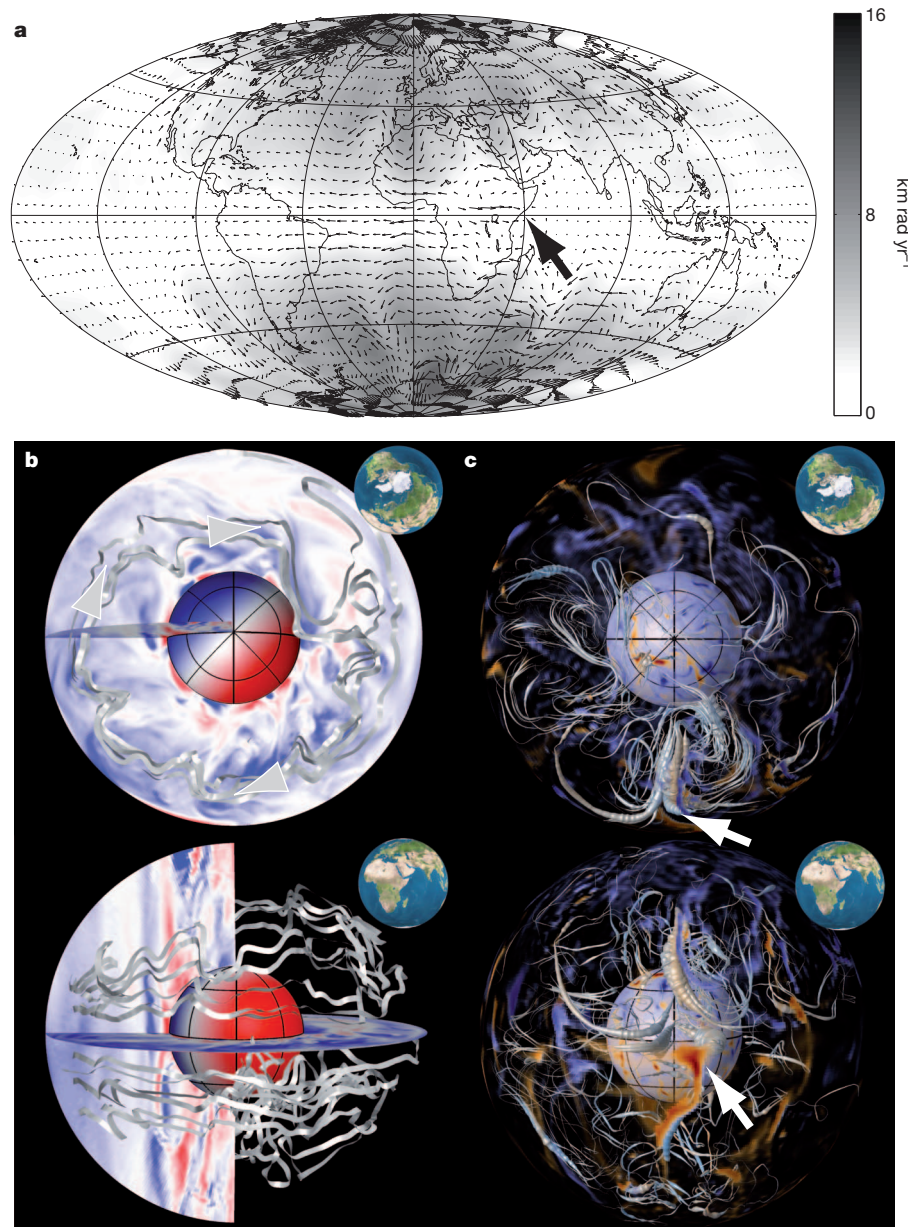


**Figure 4 | Internal fluid flow and magnetic structure.** **a**, Atlantic-centred Hammer projection of flow at the core–mantle boundary in a snapshot of the coupled Earth dynamo model (small arrows, arbitrary scaling), superimposed on a grey-scale map of the amount of local surface rotation (measured by the absolute toroidal scalar<sup>6</sup>, in  $\text{km rad yr}^{-1}$ ). The large black arrow marks the reference location introduced in Figs 2 and 3. **b**, Stream ribbon representations (top, north polar view; bottom, near-equatorial view; insets, indication of the viewing angle) of the internal velocity field structure, superimposed on equatorial and meridional cuts of the azimuthal velocity field (red is eastwards, blue is westwards, maximum  $28 \text{ km yr}^{-1}$ ). Grey arrow heads mark the general flow circulation and the twist of the ribbons is proportional to the local

vorticity. The inner-core boundary is colour-coded with the amplitude of the hemispherical modulation in mass anomaly release (red corresponds to excess buoyancy). **c**, Magnetic field line (grey) representations of the internal magnetic structure (same viewing angles as **b**). The field line thickness is proportional to the local magnetic energy density in the shell. Inner and outer boundaries are colour-coded with the amplitude of the unfiltered radial magnetic field (orange is outward, outer boundary is selectively transparent, maxima are 4 mT at the core–mantle boundary and 7 mT at the inner-core boundary). The model snapshot is taken at the same time as in Fig. 2 (which is time 0 in Fig. 3), with white arrows marking the reference location introduced in these figures.

Heterogeneous thermochemical boundary coupling is also included in the coupled Earth dynamo model. We adopt fixed-flux-type<sup>18</sup> conditions for the thermochemical buoyancy both at the core–mantle boundary (where lower-mantle thermal anomalies significantly affect the geodynamo<sup>9,20,25</sup>) and at the inner-core boundary (where solid translation of the inner core<sup>7,8</sup> can spatially modulate the inner-core growth rate, with equally important consequences<sup>6,26,27</sup>). At the core–mantle boundary, a mass anomaly flux pattern<sup>9</sup> derived from lower-mantle seismic tomography<sup>28</sup> is superimposed on a vanishing homogeneous flux. This represents a situation where the upper outer core is neutrally stratified (although

our results are robust against a possible stable stratification<sup>29,30</sup>, Supplementary Information). At the inner-core boundary, we prescribe a longitudinal hemispheric modulation of mass anomaly release related to inner-core translation. The maximum outward flux is located beneath Indonesia, in resonance with the heterogeneous mantle forcing<sup>9</sup>, and as suggested by earlier investigations<sup>6</sup>. Inner-core translation thus proceeds from east to west, opposite to inferences<sup>7</sup> based on upper inner-core seismic texturing. The latter interpretation is however not applicable here according to a parameter space exploration of our model (Supplementary Information and Extended Data Figs 2, 3), which favours

an inner-core translation slower than its mean growth rate. The upper inner-core seismic properties may thus be dominated by solidification texturing<sup>9</sup> rather than texturing induced by the slow ageing of translating iron grains.

By including these elements, the coupled Earth dynamo model is able to produce magnetic variations that are dominated by the emergence of intense, westward-drifting, equatorial flux patches of normal (the same as the ambient) polarity under the Atlantic hemisphere (Supplementary Video). The temporal sequence of emergence, drift and diffusion of these patches agrees between the model and Earth by virtue of the realistic ratio between magnetic induction and diffusion time-scales. The associated distribution of average secular variation energy (Fig. 1) quantitatively reproduces the longitudinal and latitudinal localizations of geomagnetic secular variation which standard geodynamo models fail to manage. We find (Extended Data Fig. 4) that latitudinal localization results primarily from the introduction of inner-core/mantle gravitational coupling, whereas longitudinal localization is mainly a consequence of heterogeneous thermochemical coupling between the inner and outer core. Control from the heterogeneous mantle has a secondary effect (Supplementary Information), operating constructively with the inner-core control to promote low secular variation in the Pacific<sup>20</sup>. The instantaneous field and secular variation at the core-mantle boundary exhibit detailed (Fig. 2c, d) and quantitative (Extended Data Fig. 1) agreement with present-day geomagnetic maps derived from high-resolution satellite data (Fig. 2a, b). A time-longitude plot of the evolution of radial magnetic field at the Equator from the coupled Earth dynamo model (Fig. 3a) closely resembles that obtained during the past 400 years (ref. 1; Fig. 3b), with intense patches coherently moving westwards through much of the Atlantic hemisphere, while in the Pacific hemisphere significantly weaker patches undergo slower westward drift with occasional standing and eastward-drifting phases (see also Supplementary Video). The peak of azimuthally moving power (Extended Data Fig. 5) is reached at the Equator, with a coherent westward drift at  $14 \text{ km yr}^{-1}$ , comparable to the observed speeds<sup>3</sup> of  $17 \text{ km yr}^{-1}$ . In contrast, the standard dynamo model of Fig. 1 yields a weak and erratic drift at low latitudes with a small amount of power moving slowly eastwards.

The longitudinal localization of magnetic variations in the coupled Earth dynamo model is underlain by a fluid flow (Fig. 4a, b) that agrees remarkably well with recent observation-based inferences of the core flow<sup>6,10,11</sup>. This enables a new, dynamically consistent, interpretation of the physical processes underlying such kinematic flow maps. The gyre driving the westward drift has a sheet-like structure with invariance along the Earth's rotation axis. It produces significant shear at low latitudes close to the core-mantle boundary, concentrating energetic azimuthal magnetic field lines in this region (Fig. 4c). The outer-core upwelling pattern caused by the inner-core hemispherical driving distorts the gyre into an eccentric path that reaches the core-mantle boundary beneath the Atlantic. Expulsion of azimuthal magnetic flux by columnar convection is thus strongest at this location and forms intense radial magnetic flux patches which are subsequently swept westwards by the background flow. The gyre itself is advected westwards, quasi-periodically entering into resonance with the buoyancy heterogeneity of the inner-core boundary. Its shape thus modulates between more eccentric (for example, time 0 in Fig. 3, and Figs 2 and 4) and less eccentric phases with weaker westward drift and magnetic patches more evenly distributed in longitude (for example, time 1,400 in Fig. 3). Assuming that the geodynamo is currently in a phase of more intense gyre eccentricity, our results thus indicate that advection by a planetary-scale thermochemical wind is the origin of low-latitude geomagnetic secular variation. The mechanisms identified in the coupled Earth dynamo model are generic processes related to boundary coupling and involve a competition between the Coriolis, buoyancy and magnetic forces. As realistic relative proportions of these forces are maintained in the simulation over the centennial timescale range relevant for the convective processes (Supplementary Information), these mechanisms should continue to operate in the regime of the Earth's core.

Immediate implications of our findings include the possibility of formulating a data assimilation framework based on a numerical dynamo that includes such boundary couplings. A dynamically consistent prediction of the future geomagnetic field evolution is in sight, and improved knowledge of the past of the core may be accessible through the re-analysis of historical and archaeomagnetic field data<sup>15</sup>. Our results also invite a re-evaluation of the possible strength of inner-core translation with respect to its homogeneous growth. Strong heterogeneous forcing from the inner core is in contradiction with observed geomagnetic secular variation, as it leads to core surface flows and magnetic structures with the reverse drift direction (Extended Data Fig. 3).

## METHODS SUMMARY

We solve<sup>31</sup> for Boussinesq convection, thermochemical buoyancy transport and magnetic induction in a system with constant axial rotation at a rate  $\Omega$  (defining the planetary rotating frame), comprising a spherical fluid shell between radii  $r_i$  and  $r_o$  ( $r_i/r_o = 0.35$ ), a solid inner core of radius  $r_i$  with the same electrical conductivity as the fluid shell, and an insulating solid shell representing the mantle between radii  $r_o$  and  $1.83r_o$ . The inner-core boundary is of a no-slip, electrically conducting type, and axially rotates at a rate  $\Omega_i$  under the combined influence of viscous, gravitational and magnetic torques<sup>23</sup>. The core-mantle boundary is of a free-slip, electrically insulating type and axially rotates at a rate  $\Omega_m$  under the influence of the gravitational torque. The gravitational torque on the inner core due to the mantle is given by<sup>22,23</sup>  $\Gamma_G = -\Gamma\tau(\Omega_i - \Omega_m)$ , where  $\Gamma\tau = 2.9 \times 10^{20} \text{ N m yr}$ ,  $\Gamma$  being the gravitational coupling constant and  $\tau$  the viscous relaxation time of the inner core. The inner-core boundary mass anomaly flux is fixed in the frame rotating with the mantle, with a homogeneous contribution  $f$  and a longitudinally hemispherical heterogeneity  $\Delta f = 0.8f$  maximal<sup>6</sup> at longitude  $90^\circ \text{ E}$ . The core-mantle boundary mass anomaly flux is fixed in the frame rotating with the mantle, with a vanishing homogeneous contribution and an heterogeneous pattern<sup>9</sup> derived from lower-mantle seismic tomography<sup>28</sup>, of peak-to-peak amplitude  $\Delta f_o = 0.115f$ . The Ekman number is set to  $\text{Ek} = \nu/\Omega D^2 = 3 \times 10^{-5}$  (here  $\nu$  is the fluid viscosity and  $D = r_o - r_i$  is the fluid shell depth). The mass anomaly flux Rayleigh number is  $\text{Ra}_f = g_o f / \rho \Omega^3 D^2 = 9.3 \times 10^{-5}$  (here  $g_o$  is the gravity at the core-mantle boundary and  $\rho$  is the fluid density). The ratios between the fluid viscosity, thermal diffusivity  $\kappa$  and magnetic diffusivity  $\lambda$  are set to  $\text{Pr} = \nu/\kappa = 1$  and  $\text{Pr}_m = \nu/\lambda = 2.5$  (here  $\text{Pr}$  and  $\text{Pr}_m$  are respectively the Prandtl number and the magnetic Prandtl number). The non-dimensional model output is rescaled to the dimensional world using scaling principles thought to hold in both model and Earth: secular variation time scaling<sup>32</sup> and convective-power-based magnetic field scaling<sup>33</sup>.

**Online Content** Any additional Methods, Extended Data display items and Source Data are available in the online version of the paper; references unique to these sections appear only in the online paper.

Received 26 March; accepted 14 August 2013.

- Jackson, A., Jonkers, A. R. T. & Walker, M. R. Four centuries of geomagnetic secular variation from historical records. *Phil. Trans. R. Soc. Lond. A* **358**, 957–990 (2000).
- Holme, R., Olsen, N. & Bairstow, F. L. Mapping geomagnetic secular variation at the core-mantle boundary. *Geophys. J. Int.* **186**, 521–528 (2011).
- Finlay, C. C. & Jackson, A. Equatorially dominated magnetic field change at the surface of Earth's core. *Science* **300**, 2084–2086 (2003).
- Christensen, U. R., Aubert, J. & Hulot, G. Conditions for Earth-like geodynamo models. *Earth Planet. Sci. Lett.* **296**, 487–496 (2010).
- Buffett, B. Gravitational oscillations in the length of day. *Geophys. Res. Lett.* **23**, 2279–2282 (1996).
- Aubert, J. Flow throughout the Earth's core inverted from geomagnetic observations and numerical dynamo models. *Geophys. J. Int.* **192**, 537–556 (2013).
- Monnereau, M., Calvet, M., Margerin, L. & Souriau, A. Lopsided growth of Earth's inner core. *Science* **328**, 1014–1017 (2010).
- Alboussière, T., Deguen, R. & Melzani, M. Melting-induced stratification above the Earth's inner core due to convective translation. *Nature* **466**, 744–747 (2010).
- Aubert, J., Amit, H., Hulot, G. & Olson, P. Thermochemical flows couple the Earth's inner core growth to mantle heterogeneity. *Nature* **454**, 758–761 (2008).
- Pais, M. A. & Jault, D. Quasi-geostrophic flows responsible for the secular variation of the Earth's magnetic field. *Geophys. J. Int.* **173**, 421–443 (2008).
- Gillet, N., Pais, M. A. & Jault, D. Ensemble inversion of time-dependent core flow models. *Geochim. Geophys. Geosyst.* **10**, Q06004 (2009).
- Olsen, N., Manda, M., Sabaka, T. J. & Toffner-Clausen, L. The CHAOS-3 geomagnetic field model and candidates for the 11th generation IGRF. *Earth Planets Space* **62**, 719–727 (2010).
- Lesur, V., Wardinski, I., Hamoudi, M. & Rother, M. The second generation of the GFZ Reference Internal Magnetic Model: GRIMM-2. *Earth Planets Space* **62**, 765–773 (2010).

14. Finlay, C. C., Jackson, A., Gillet, N. & Olsen, N. Core surface magnetic field evolution 2000–2010. *Geophys. J. Int.* **189**, 761–781 (2012).
15. Fournier, A. et al. An introduction to data assimilation and predictability in geomagnetism. *Space Sci. Rev.* **155**, 247–291 (2010).
16. Christensen, U. R. & Wicht, J. in *Treatise on Geophysics* Vol. 8, *Core Dynamics* (ed. Schubert, G.) Ch. 8 (Elsevier, 2007).
17. Kuang, W. & Bloxham, J. An Earth-like numerical dynamo model. *Nature* **389**, 371–374 (1997).
18. Sakuraba, A. & Roberts, P. H. Generation of a strong magnetic field using uniform heat flux at the surface of the core. *Nature Geosci.* **2**, 802–805 (2009).
19. Miyagoshi, T., Kageyama, A. & Sato, T. Zonal flow formation in the Earth's core. *Nature* **463**, 793–796 (2010).
20. Christensen, U. R. & Olson, P. Secular variation in numerical geodynamo models with lateral variations of boundary heat flux. *Phys. Earth Planet. Inter.* **138**, 39–54 (2003).
21. Glatzmaier, G. A. & Roberts, P. H. Rotation and magnetism of Earth's inner core. *Science* **274**, 1887–1891 (1996).
22. Buffett, B. A. & Glatzmaier, G. A. Gravitational braking of inner-core rotation in geodynamo simulations. *Geophys. Res. Lett.* **27**, 3125–3128 (2000).
23. Aubert, J. & Dumberry, M. Steady and fluctuating inner core rotation in numerical geodynamo models. *Geophys. J. Int.* **184**, 162–170 (2011).
24. Dumberry, M. Geodynamic constraints on the steady and time-dependent inner core axial rotation. *Geophys. J. Int.* **170**, 886–895 (2007).
25. Gubbins, D., Sreenivasan, B., Mound, J. & Rost, S. Melting of the Earth's inner core. *Nature* **473**, 361–363 (2011).
26. Davies, C. J., Silva, L. & Mound, J. E. On the influence of a translating inner core in models of outer core convection. *Phys. Earth Planet. Inter.* **214**, 104–114 (2013).
27. Olson, P. & Deguen, R. Eccentricity of the geomagnetic dipole caused by lopsided inner core growth. *Nature Geosci.* **5**, 565–569 (2012).
28. Masters, G., Laske, G., Bolton, H. & Dziewonski, A. in *Earth's Deep Interior* (eds Karato, S., Forte, A., Liebermann, R. C., Masters, G. & Stixrude, L.) 63–87 (AGU Monograph Vol. 117, American Geophysical Union, 2000).
29. Helffrich, G. & Kaneshima, S. Outer-core compositional stratification from observed core wave speed profiles. *Nature* **468**, 807–810 (2010).
30. Gubbins, D. & Davies, C. J. The stratified layer at the core-mantle boundary caused by baro-diffusion of oxygen, sulphur and silicon. *Phys. Earth Planet. Inter.* **215**, 21–28 (2013).
31. Aubert, J., Labrosse, S. & Poitou, C. Modelling the palaeo-evolution of the geodynamo. *Geophys. J. Int.* **179**, 1414–1428 (2009).
32. Lhuillier, F., Fournier, A., Hulot, G. & Aubert, J. The geomagnetic secular-variation timescale in observations and numerical dynamo models. *Geophys. Res. Lett.* **38**, L09306 (2011).
33. Christensen, U. R. & Aubert, J. Scaling properties of convection-driven dynamos in rotating spherical shells and application to planetary magnetic fields. *Geophys. J. Int.* **166**, 97–114 (2006).

**Supplementary Information** is available in the online version of the paper.

**Acknowledgements** This work was supported by the French Agence Nationale de la Recherche (grant ANR-2011-BS56-011). Numerical computations were performed at S-CAPAD, IPGP, France, and using HPC resources from GENCI-IDRIS (grants 2012-042122 and at 2013-042122). This is IPGP contribution 3419.

**Author Contributions** J.A. designed the project and carried out the numerical experiments. J.A. and C.C.F. designed the numerical experiments and processed the results. J.A., C.C.F. and A.F. discussed the results and commented on the manuscript.

**Author Information** Reprints and permissions information is available at [www.nature.com/reprints](http://www.nature.com/reprints). The authors declare no competing financial interests. Readers are welcome to comment on the online version of the paper. Correspondence and requests for materials should be addressed to J.A. ([aubert@ipgp.fr](mailto:aubert@ipgp.fr)).

## METHODS

**Model description.** The model solves for Boussinesq convection, thermochemical buoyancy transport and magnetic induction in the magnetohydrodynamic approximation in an electrically conducting spherical fluid shell with inner and outer radii  $r_i$  and  $r_o$  (in constant ratio  $r_i/r_o = 0.35$ , as in the present Earth's core aspect ratio; equations are described in ref. 31). This fluid shell is coupled to a solid inner core of radius  $r_i$  with the same electrical conductivity as the fluid shell, itself coupled to an insulating solid spherical shell between radii  $r_o$  and  $1.83r_o$  representing the mantle. The whole system has a constant axial rotation rate  $\Omega$  defining the planetary rotating frame, such that:

$$I_i\Omega_i + I_{oc}\Omega_{oc} + I_m\Omega_m = (I_i + I_{oc} + I_m)\Omega \quad (1)$$

Here  $I_i$ ,  $I_{oc}$  and  $I_m$  are respectively the axial moments of inertia of the inner core, the fluid outer core and the mantle, with values<sup>34</sup>  $I_i = 5 \times 10^{34} \text{ kg m}^2$ ,  $I_{oc} = 0.9 \times 10^{37} \text{ kg m}^2$  and  $I_m = 7.1 \times 10^{37} \text{ kg m}^2$ ;  $\Omega_i$ ,  $\Omega_{oc}$  and  $\Omega_m$  are respectively the solid body rotation rates of the inner core, the fluid outer core and the mantle. Electrically conducting and no-slip boundary conditions are adopted at the inner-core boundary, which rotates axially under the combined influence of viscous, gravitational and magnetic torques. Our implementation of inner-core rotation and torques follows that of ref. 23 except for the fact that the mantle also rotates axially. For angular rotations occurring on timescales longer than the viscous relaxation time  $\tau$  of the inner core, the gravitational torque on the inner core due to the mantle is then given by<sup>22</sup>

$$\Gamma_G = -\Gamma\tau(\Omega_i - \Omega_m) \quad (2)$$

where  $\Gamma$  is the gravitational coupling constant. The product  $\Gamma\tau$  is set to the value  $2.9 \times 10^{20} \text{ N m yr}$ , obtained by comparing the recent core-originated variations in the length of the day with predictions<sup>6</sup> from inverted core flows using our numerical dynamo model as a statistical prior (Extended Data Fig. 2). Electrically insulating and free-slip boundary conditions are adopted at the axially rotating core-mantle boundary. The evolution equation for  $\Omega_m$  then gives:

$$I_m \frac{d\Omega_m}{dt} = -\Gamma_G \quad (3)$$

The angular momentum conservation in the coupled core-mantle-inner-core system identically follows from this formulation. Our choice to ignore direct coupling between the outer core and the mantle implies vanishing long-term gravitational torque and steady inner-core differential rotation ( $\Omega_i - \Omega_m = 0$  averaged over time) relative to the mantle from equations (2) and (3). Relative to the planetary rotating frame, the outer-core westward drift (negative  $\Omega_{oc} - \Omega$ ) obtained in steady-state is compensated by a weak permanent eastward rotation (positive  $\Omega_m - \Omega$ ) of the mantle and inner core. This latter rotation can be cancelled by choosing a new frame of reference in which all the present results are expressed. The long-term torque exerted by the outer core on the inner core also vanishes as it balances the long-term gravitational torque.

**Boundary conditions for buoyancy.** The mass anomaly flux at the inner-core boundary is fixed, with an homogeneous flux per unit surface  $f$  and a longitudinal hemispheric heterogeneity with peak-to-peak magnitude  $\Delta f = 0.8f$ , the maximum of which is kept at a fixed longitude  $90^\circ \text{ E}$  relative to the mantle<sup>6</sup>. This is a reasonable simplification as the angular shift between the inner core and the mantle never exceeds  $5^\circ$  in the simulation. The mass anomaly flux at the core-mantle boundary is fixed in the frame rotating with the mantle, with a vanishing homogeneous component and an heterogeneous pattern derived from lower-mantle

seismic tomography<sup>28</sup> (same pattern as in ref. 9). A volumetric buoyancy sink term is present in the Boussinesq thermochemical transport equation<sup>31</sup> in order to ensure mass conservation. The peak-to-peak amplitude  $\Delta f_o$  of the core-mantle boundary heterogeneity is chosen such that the corresponding heat flow heterogeneity amplitude is  $\Delta q = 1.5q_{ad}$  (this probably overestimates the influence of the mantle, see Supplementary Information), where  $q_{ad}$  is the core-mantle boundary adiabatic heat flow per unit surface. Balancing the rate of dissipation with the perfect-mixing gravitational energy release<sup>31</sup> yields, in a situation without core radioactive heating:

$$4\pi r_o^2(\varepsilon_L + \varepsilon_B)q_{ad} = 4\pi r_i^2(\bar{\Psi} - \Psi_i)f \quad (4)$$

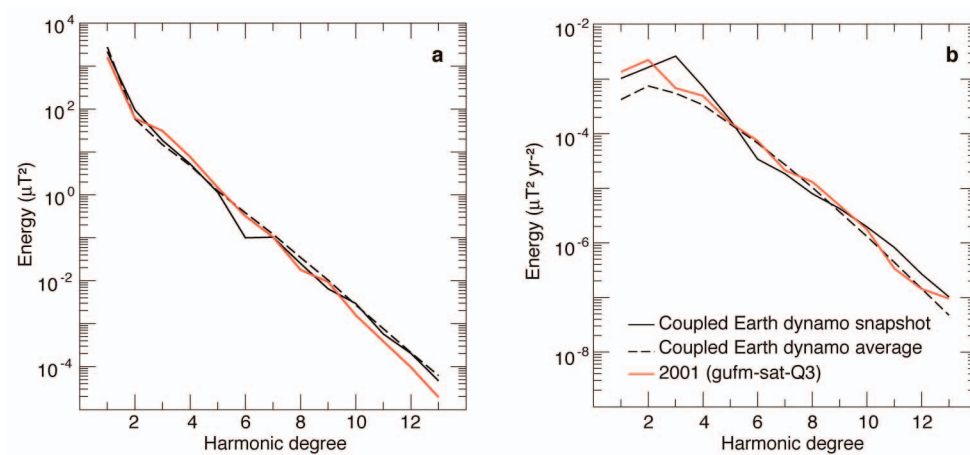
Here<sup>31</sup>  $\varepsilon_L + \varepsilon_B = 0.2$  is the combined thermodynamical efficiency of latent heat and light element release, and  $\bar{\Psi} - \Psi_i = 10^7 \text{ m}^2 \text{ s}^{-2}$  is the difference between the inner-core boundary and average outer-core gravitational potential. We also have  $\Delta f_o = \alpha\Delta q/C_p$ , where<sup>31</sup>  $\alpha = 10^{-5} \text{ K}^{-1}$  and  $C_p = 800 \text{ J K}^{-1} \text{ kg}^{-1}$  are respectively the fluid thermal expansion coefficient and heat capacity. Finally, we numerically implement the following ratio:

$$\frac{\Delta f_o}{f} = \frac{\alpha r_i^2}{C_p r_o^2} \left( \frac{\bar{\Psi} - \Psi_i}{\varepsilon_L + \varepsilon_B} \right) \frac{\Delta q}{q_{ad}} = 0.115 \quad (5)$$

**Model fundamental parameters and numerical method.** The Ekman number is set to  $Ek = \nu/\Omega D^2 = 3 \times 10^{-5}$  (here  $\nu$  is the fluid viscosity and  $D = r_o - r_i$  is the fluid shell depth). The mass anomaly flux Rayleigh number is  $Ra_f = g_o f l \rho \Omega^2 D^2 = 9.3 \times 10^{-5}$  (here  $g_o$  is the gravity at the core-mantle boundary and  $\rho$  is the fluid density). The Prandtl and magnetic Prandtl ratios between the fluid viscosity, thermal and magnetic diffusivities  $\kappa$ ,  $\lambda$  are set to  $Pr = \nu/\kappa = 1$  and  $Pr_m = \nu/\lambda = 2.5$ . With such parameters, the model produces a non-reversing magnetic field with Earth-like morphology<sup>4</sup>. The numerical implementation decomposes the fields in spherical harmonics up to degree and order 133, and discretizes them in the radial direction on a second-order finite differencing scheme with 160 points non-uniformly distributed in radius. Time-stepping is of second-order, semi implicit type. Angular momentum conservation is controlled at each time step. The model is initialized using a thermochemical perturbation, zero velocity field and an axially dipolar magnetic field. After the time needed for equilibration, the model is integrated over half a magnetic diffusion time.

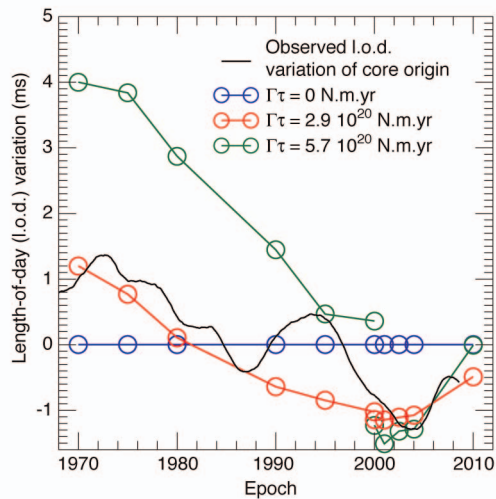
**Rescaling of model dimensionless quantities.** Non-dimensional length is rescaled to the dimensional world using the unit length  $D = 2,260 \text{ km}$  (the depth of Earth's core). Non-dimensional time is rescaled by matching the model secular variation timescale to the geomagnetic secular variation timescale<sup>32</sup> (procedure details in ref. 6). As the model magnetic Reynolds number is comparable to the Earth target (Extended Data Table 1 and Supplementary Information), this is roughly similar to matching the model magnetic diffusion timescale to its Earth value. This is also effectively similar to expressing the model viscous diffusion time with an exaggerated fluid turbulent viscosity  $\nu = 2.9 \text{ m}^2 \text{ s}^{-1}$ . The non-dimensional magnetic field is rescaled to the dimensional world by matching the model and Earth predictions obtained with the convective-power based magnetic field scaling<sup>33</sup> (procedure details also in ref. 6).

34. Ahrens, T. J. *Global Earth Physics: A Handbook of Physical Constants* Vol. 1 (AGU, 1995).
35. Sabaka, T. J., Olsen, N. & Purucker, M. Extending comprehensive models of the Earth's magnetic field with Oersted and CHAMP data. *Geophys. J. Int.* **159**, 521–547 (2004).

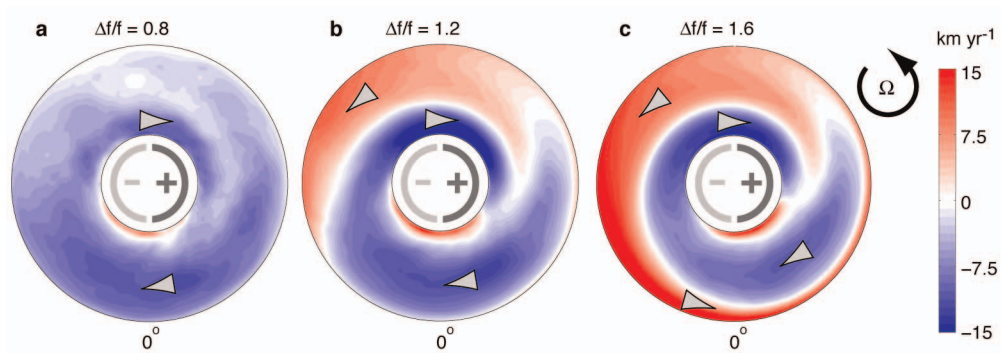


**Extended Data Figure 1 | Energy spectra of the coupled Earth dynamo.**  
**a, b,** Earth-surface energy spectra for the magnetic field (**a**) and secular variation (**b**), as functions of spherical harmonic degree. The geomagnetic field model<sup>14</sup> gufm-sat-Q3 in 2001 is given as a red line (corresponding to Fig. 2a, b),

together with a snapshot of the coupled Earth dynamo model (solid black line, same time as Fig. 2c, d) and its time-averaged spectrum (dashed black line, averaging time is 67,000 years).

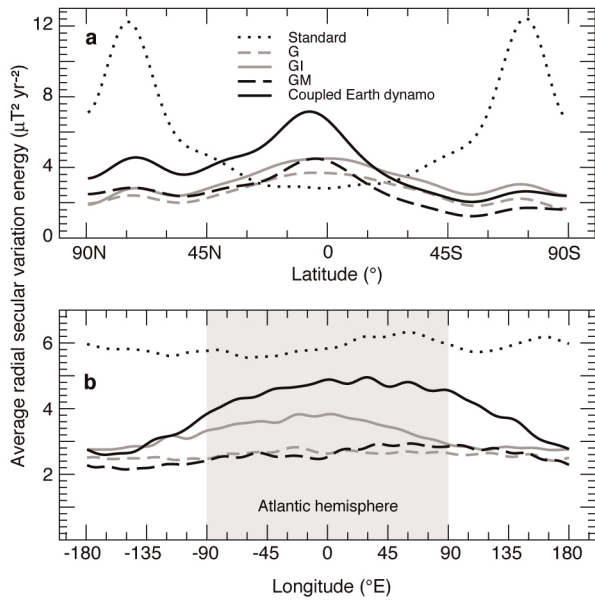


**Extended Data Figure 2 | Variations in the length of day arising from core–mantle angular momentum exchanges.** The optimal choice for the model gravitational coupling constant  $\Gamma\tau$  (Methods) is guided by inverting geomagnetic field model<sup>35</sup> CM4 between 1960 and 2000, and model<sup>14</sup> gufm-sat-Q3 between 2000 and 2010, for length-of-day variations (open circles), using an inverse geodynamo modelling framework (see figure 13 in ref. 6 and associated discussion for a full description of the method). The prior numerical dynamo models used in the framework (Extended Data Table 1) are G (green line) and GI (red line). A vanishing gravitational coupling results in vanishing length-of-day variations (blue line). Variations in Earth’s length of day of core origin (as computed in ref. 11) are represented in black.

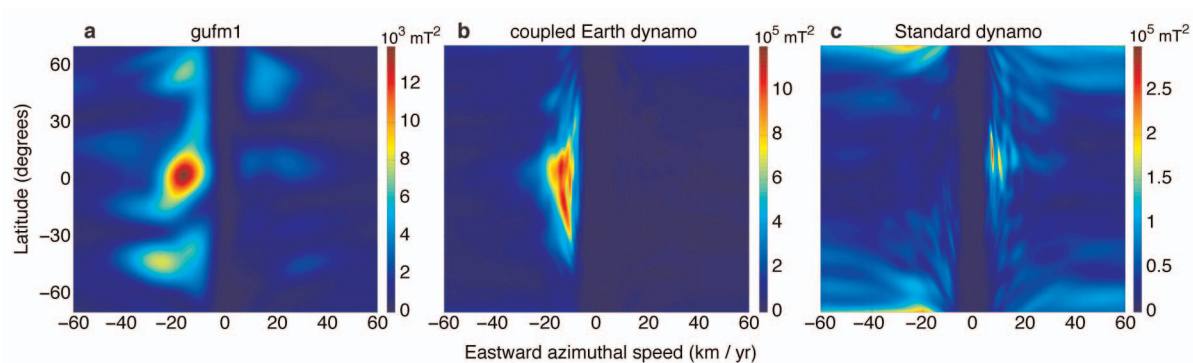


**Extended Data Figure 3 | Effect of the inner-core boundary mass anomaly flux heterogeneity.** Time-averaged plots of azimuthal velocity in the equatorial plane (blue is westwards, grey arrows mark the general circulation) for models G1, G1.2 and G1.6 (respectively a–c, Extended Data Table 1) where

the amplitude  $\Delta f/f$  of the inner-core boundary heterogeneity is varied. The grey half-circles represent the orientation of the hemispherical buoyancy release heterogeneity at the inner boundary. The location of the Greenwich meridian ( $0^\circ$ ) is also marked.



**Extended Data Figure 4 | Origin of the geographical localization of secular variation.** Longitudinally (a) and latitudinally (b) averaged profiles of the time average secular variation energy contained in models G, GI, GM, the standard and the coupled Earth dynamo models (Extended Data Table 1). Secular variation is filtered at spherical harmonic degree and order 8, as in Fig. 1.



**Extended Data Figure 5 | Analysis of longitudinal magnetic drift.** Shown is magnetic power coherently moving in the longitudinal direction, as a function of latitude and azimuthal speed. **a**, Analysis of the historical field model gufm1 following ref. 3. **b**, **c**, Same analysis, applied respectively to 3,000-year sequences of the coupled Earth and standard dynamo models, filtered at spherical harmonic degree and order 13. Power colour scale differs in **a**, **b** and **c** owing to the different timespans available in the dynamo models and the historical geomagnetic field model. The analysis is performed using the Radon transform technique (Supplementary Information).

Extended Data Table 1 | Model parameter-space exploration.

Model	Boundaries	$Re_m = \frac{\tau_\lambda}{\tau_U}$	$Ek_m = \frac{1}{\Omega\tau_\lambda}$	$\frac{\Gamma\tau}{\rho D^3\nu}$	$\Delta f/f$	$\Delta f_o/f$	$\chi^2$
Standard	Type 0	858	$1.2 \cdot 10^{-5}$	0	0	0	1
G	Type 1	982	$1.2 \cdot 10^{-5}$	$5 \cdot 10^4$	0	0	0.8
GS	Type 2	1,066	$1.2 \cdot 10^{-5}$	$2.5 \cdot 10^4$	0	0	2.4
GI	Type 1	965	$1.2 \cdot 10^{-5}$	$2.5 \cdot 10^4$	0.8	0	1.2
GI1.2	Type 1	989	$1.2 \cdot 10^{-5}$	$2.5 \cdot 10^4$	1.2	0	2.4
GI1.6	Type 1	996	$1.2 \cdot 10^{-5}$	$2.5 \cdot 10^4$	1.6	0	2.4
GM	Type 1	967	$1.2 \cdot 10^{-5}$	$2.5 \cdot 10^4$	0	0.115	0.1
Coupled Earth	Type 1	942	$1.2 \cdot 10^{-5}$	$2.5 \cdot 10^4$	0.8	0.115	0.6

Shown are parameters of the numerical models integrated in addition to the coupled Earth and standard dynamo models, and discussed in Supplementary Information. All models have the same Rayleigh, Ekman, Prandtl and magnetic Prandtl numbers, as defined in Methods. Type 0 refers to mechanically rigid, electrically insulating and fixed boundaries in the planetary rotating frame, type 1 refers to no-slip, axially rotating planetary and electrically conducting inner boundary, free-slip, axially rotating and electrically insulating outer boundary. For types 0 and 1, the mass anomaly flux is fixed in the mantle rotating frame at both boundaries (the homogeneous mass anomaly flux vanishes at the outer boundary). Type 2 is similar to type 1, but with an inward homogeneous mass anomaly flux at the outer boundary amounting to one-third of the flux emerging from the inner boundary (stratified upper outer core situation). The magnetic Reynolds number  $Re_m$  and magnetic Ekman number  $Ek_m$  compare the magnetic diffusion timescale  $\tau_\lambda$ , the core overturn time  $\tau_U$  and the inverse rotation rate  $1/\Omega$ . The quantity  $\chi^2$  is an attempt to measure the static morphological semblance<sup>4</sup> of the model magnetic field output to the geomagnetic field (values lower than 2 indicate excellent semblance).

## 1 Parameter space exploration and rationale for parameter choices

Here we give a detailed account of the parameter space exploration (Extended Data Table 1) carried out in support of the coupled Earth dynamo model presented in the main text. We also justify the parameter choices which have prevailed in designing this model. Across the parameter space, we mainly vary the gravitational coupling constant, inner core and core-mantle boundary buoyancy heterogeneity amplitude, and amount of stratification at the core-mantle boundary since the more fundamental parameters are set by the requirement (systematically documented elsewhere<sup>1</sup>) to simulate magnetic fields with Earth-like morphologies.

**Morphological similarity of the simulated and geomagnetic field and secular variation.** The magnetic fields in all models except those exploring strong inner core boundary heterogeneity amplitudes (GI1.2 and GI1.6) and upper outer core stratification (GS) are morphologically similar to the geomagnetic field, as witnessed by the low values  $\chi^2 \leq 2$  of their quantitative similarity assessment<sup>1</sup> (Extended Data Table 1). This generally follows<sup>1</sup> from our choices for the magnetic Reynolds number  $Re_m$  and magnetic Ekman number  $Ek_m$ , which compare the model magnetic diffusion, core overturn and planetary rotation time scales. These have been maintained as close as was computationally feasible to their Earth targets  $Re_m = UD/\lambda \approx 900 - 2000$  and  $Ek_m = \lambda/\Omega D^2 \approx 1 - 3 \cdot 10^{-9}$ , obtained with a magnetic diffusivity<sup>2,3</sup>  $\lambda \approx 0.5 - 1.2 \text{ m}^2/\text{s}$ , typical core flow velocity  $U \approx 5 \cdot 10^{-4} \text{ m/s}$ , outer core width  $D = 2260 \text{ km}$  and rotation rate  $\Omega = 7.29 \cdot 10^{-5} \text{ rad/s}$ . Extended Data Figure 1 provides further details of the quantitative similarity between the coupled Earth dynamo model output and the geomagnetic field and secular variation.

While most models summarised in Extended Data Table 1 reproduce the observed amplitude<sup>4</sup> of the geomagnetic westward drift, two important cases fail to meet this requirement: the standard model, where equatorial magnetic structures have a weak and erratic drift (see Extended Data Figure 5), and the strong inner core boundary heterogeneity model GI1.6, where the inner core forcing induces a planetary-scale eastward flow below the core-mantle boundary (see Extended Data Figure 3).

**Magnetic-Archimedes-Coriolis force balance in the model and in the Earth's core.** For computational reasons, the planetary rotation rate used in all models is too slow since the model magnetic Ekman number  $Ek_m$  is four order of magnitudes larger than its target value. For large flow scales and over time scales relevant to the secular variation, the Coriolis force is nevertheless in realistic proportion with the magnetic force, as witnessed by the dynamical Elsasser ratio<sup>5</sup>

$$\Lambda_d = \frac{(\nabla \times \mathbf{B}) \times \mathbf{B}}{\rho\mu_0|\boldsymbol{\Omega} \times \mathbf{u}|} \approx \frac{B^2 t}{\rho\mu_0\Omega D^2}. \quad (1)$$

Here  $\mathbf{B}$  and  $\mathbf{u}$  are the magnetic and velocity fields in the shell, and  $t$  the time scale of interest. The coupled Earth model dynamical Elsasser numbers are  $\Lambda_d = O(10^{-2})$  at the core overturn time scale  $t = \tau_U = D/U$  and  $\Lambda_d = O(1)$  at the magnetic diffusion time scale  $t = \tau_\lambda = D^2/\lambda$ , where the

dynamical Elsasser number then coincides with the classical Elsasser number  $B^2/\rho\lambda\mu_0\Omega$ . Similar values are obtained for the Earth's core using<sup>6,7</sup>  $B = 2.5$  mT and  $\rho = 11000$  kg/m<sup>3</sup>. The Coriolis force is also in realistic proportion with the buoyancy force, as shown by the ratio

$$Bu = \frac{|g_o C|}{\rho|\boldsymbol{\Omega} \times \mathbf{u}|} \approx \frac{g_o f}{\rho\Omega U^2}. \quad (2)$$

Here  $C \approx f/U$  is the typical co-density perturbation present in the fluid. The coupled Earth dynamo model has  $Bu = 0.8$  while  $Bu = 0.6$  is expected in the core based on a mass anomaly flux<sup>6</sup> per unit inner core surface  $f \approx 10^{-8}$  kg/(m<sup>2</sup>s), and  $g_o = 10$  m/s<sup>2</sup>. Values  $Bu = O(1)$  are incidentally representative of the thermochemical wind equilibrium<sup>8</sup> driving the westward drift. Given the realistic proportions of the Coriolis, buoyancy and magnetic forces, the predominantly columnar flow obtained in the model (Figure 4) at time scales comparable to  $\tau_U$ , with deviations from columnarity at time scales comparable to  $\tau_\lambda$  is thus expected to be representative of the geodynamo. As with all three-dimensional convective dynamo models, the relative amplitude of the viscous, inertial and Coriolis force is not representative of the Earth's core. Inertia and viscosity nevertheless have a minor influence compared to the Coriolis force (as is the case in the core), as witnessed by the ratios  $Ro = U/\Omega D \approx 10^{-2}$  and  $Ek = \nu/\Omega D^2 = 3 \cdot 10^{-5}$ . It can thus be expected that they do not significantly influence the mechanism proposed in the main text for the westward drift, which relies on the primary balance between the Coriolis, magnetic and buoyancy forces.

**Choice of gravitational coupling constant using length-of-day variations.** In a previously published inverse modelling framework<sup>9</sup>, we have shown how inversions for flow throughout the core can be obtained by using a numerical dynamo model as statistical prior. Length-of-day variations of core origin can then be computed and compared with geodetic data<sup>10</sup>. In our model, gravitational coupling is the only source of angular momentum exchanges between the core and the mantle. Comparing predicted and observed variations of the length-of-day then provides a quantitative test bed for the gravitational coupling constant  $\Gamma\tau$  (Extended Data Table 1) used in the model. Here we use two of our models (G and GI) as inversion priors (which implies a detailed computation of their multivariate statistics), and provide in Extended Data Figure 2 an updated version of Figure 13 from ref. <sup>9</sup>. In this figure, the dimensional equivalents of the nondimensional gravitational coupling constants are obtained through our usual re-scaling principles (Methods). Extended Data Figure 2 shows that the choice  $\Gamma\tau = 5.7 \cdot 10^{20}$  N.m.yr made in model G overestimates the core-originated variations in the length of day between 1970 and 2010, while the choice  $\Gamma\tau = 2.9 \cdot 10^{20}$  N.m.yr made in other models (including the coupled Earth dynamo) reasonably estimates both the amplitude and the long-term trend of these variations.

Cancelling the gravitational coupling between the inner core and the mantle (blue line in Extended Data Figure 2) annihilates the steady westward drift in the outer core, which then becomes erratic as in most standard dynamo models<sup>11</sup>, while the inner core steadily rotates in the eastward direction<sup>12</sup> with respect to the mantle. Nonvanishing values of  $\Gamma\tau$  automatically imply long-term corotation of the inner core and the mantle (but the duration of the transients leading to the long-term state is inversely proportional to  $\Gamma\tau$ ), and the steady outer core westward drift is then limited by the strength of thermo-chemical wind shears.

**Choice of inner-core boundary buoyancy heterogeneity and slow inner core translation.** The above determined value for the gravitational coupling constant sets a constraint on the viscous relaxation time  $\tau$  of the inner core<sup>13</sup>. Recent estimates of the mantle geoid suggest  $\Gamma = 3 \times 10^{19} - 3 \times 10^{20}$  N.m (refs. <sup>14,15</sup> and references therein). Our preferred value is then  $\tau = 1 - 10$  yr, compatible with a previous independent determination<sup>16</sup>. The corresponding<sup>13</sup> inner core viscosity range  $\eta = 5 \times 10^{16} - 5 \times 10^{17}$  Pa.s partially overlaps the range<sup>17,18</sup>  $\eta = 10^{17} - 4 \times 10^{18}$  Pa.s over which the translational instability of the inner core is hampered by its viscous deformation. This is the first of two results leading us to favour the hypothesis of slow inner core translation made in the main text. In the coupled Earth dynamo model, the ratio  $\Delta f/f = 0.8$  of the hemispherical modulation of the inner core mass anomaly flux to its homogeneous component is representative of this hypothesis. This ratio is indeed approximately equal to<sup>6,19</sup>  $2v_i/\dot{r}_i$  where  $v_i$  is the translation velocity and  $\dot{r}_i$  the homogeneous inner core growth rate. We have also investigated the influence of stronger inner core buoyancy heterogeneities (models GI1.2 and GI1.6, Extended Data Figure 3). We found that well below the forcing  $\Delta f/f = 2$  at which the inner core translation speed exceeds its growth rate, the agreement between the model output and geomagnetic observations significantly degrades, in terms of static field morphology ( $\chi^2$  values in Extended Data Table 1), secular variation (the magnetic drift direction globally turns eastwards in GI1.6) and flow similarity to whole core flow inversions<sup>9,10,20</sup>. This second result reinforces our hypothesis of a slow inner core translation velocity relatively to its mean growth rate.

The existence of inner core translation requires an unstable density stratification within the inner core<sup>21,22</sup>. However, within the framework of the above hypothesis, density stratification should only be marginally unstable, otherwise translation speeds may exceed the inner core growth rate, or translation may become subdominant with respect to other inner core convective modes<sup>18</sup>. In the Earth's inner core, this situation may arise from the competition between stable thermal density gradients arising from the large thermal conductivity of iron and insufficient inner core boundary heat flow<sup>3</sup> and unstable chemical density gradients created by the variable partitioning of light elements between the solid and liquid as the inner core grows<sup>23</sup>.

**Choice of homogeneous core-mantle boundary heat flow and possible upper outer core stratification.** The coupled Earth dynamo model has neutral average buoyancy at the core-mantle-boundary, representing a situation where the homogeneous part of heat flow  $Q$  at this boundary is exactly adiabatic. Given recent first-principle calculations<sup>3,24</sup> yielding an adiabatic core heat flow  $Q_{ad} = 15$  TW, our hypothesis favours a value for  $Q$  at the upper bound of the range 7.5 – 15 TW suggested by extrapolations of local estimates<sup>25,26</sup>. In order to account for the possibility that the upper outer core is stably stratified<sup>27,28</sup>, model GS explores the situation where  $Q = 10$  TW, in the absence of core internal radioactive heating. This situation is approximated in the Boussinesq framework used in our model by imposing a negative mass anomaly flux  $F_o$  at the core-mantle boundary. Perfect-mixing relationships<sup>6</sup> already introduced in Methods yield the following ratio between  $F_o$  and the total inner core mass anomaly flux  $F$ :

$$\frac{F_o}{F} = \frac{\alpha}{C_p} \left( \frac{\bar{\Psi} - \Psi_i}{\epsilon_L + \epsilon_B} \right) \frac{Q - Q_{ad}}{Q}. \quad (3)$$

Using the values introduced in Methods then leads to prescribing  $F_o/F = -1/3$  in model GS. The corresponding turning point for the thermochemical gradient (the point where the background profile turns from unstable to stable) is then found to be located at 250 km below the core surface, in agreement with other recent thermodynamical models<sup>3</sup> and with a seismically inferred<sup>27</sup> depth for the stratified region. The strength of stratification is measured by the buoyancy frequency  $N$ , which, relative to the inverse magnetic diffusion time  $\lambda/D^2$ , writes

$$ND^2/\lambda = \frac{D^2}{\lambda} \sqrt{-\frac{g}{\rho} \frac{\partial \rho}{\partial r}} = \sqrt{\frac{-Ra_{Fo} Pr_m^2 Pr}{Ek^3}}. \quad (4)$$

Here  $Ra_{Fo} = \frac{Fo}{F} \left(\frac{r_i}{r_o}\right)^2 Ra_F$  is the negative Rayleigh number pertaining to the stable CMB stratification. Our parameter set for model GS yields  $ND^2/\lambda \approx 3 \cdot 10^4$ . Using the previously mentioned estimates for the magnetic diffusivity, this finally yields  $N = O(10^{-5})$  mHz, five orders of magnitude smaller than the seismologically inferred estimates<sup>27</sup>. Convective dynamo numerical codes are indeed limited by the validity range of the Boussinesq approximation in which they are formulated, and by numerical difficulties associated with resolving fast transients in strongly stratified environments. We note however that  $N\tau_U \approx 30$ , meaning that the modelled layer is reasonably resistant to radial fluid transport.

We found that the morphological agreement between model GS and the geomagnetic field is degraded with respect to results obtained with the coupled Earth dynamo ( $\chi^2$  values in Extended Data table 1). Model GS however produces low-latitude, westward drifting equatorial magnetic flux patches, with the same properties and underlying mechanisms as the coupled Earth dynamo. Our interpretation of this robustness ties with the long temporal coherence (millennial time scales, Figure 3) of these patches. This coherence is indeed long-lasting enough for the associated electromagnetic skin depth to match the core stratification depth, in which case the magnetic patches can diffuse through the stratified layer.

**Choice of the amplitude of core-mantle boundary heat flow heterogeneity.** Local estimates of the core-mantle boundary heat flow<sup>25,26</sup> suggest a peak-to-peak amplitude for the mantle-driven heat flow heterogeneity at  $\Delta q \approx 40$  mW/m<sup>2</sup>, and a ratio  $\Delta q/q_{ad} \approx 0.4$  relatively to the adiabatic heat flow<sup>3</sup> per unit surface  $q_{ad} = 100$  mW/m<sup>2</sup>. In the coupled Earth dynamo model, this ratio is overestimated since the local mass anomaly flux heterogeneity  $\Delta f_o$  is set respectively to the inner core flux  $f$  such that  $\Delta q/q_{ad} = 1.5$  (Methods). This overestimation of the top-down forcing from the core-mantle boundary is intentional and meant to highlight the dominance of bottom-up heterogeneous forcing from the inner core boundary.

**Role of the inner core and mantle in the geographical localisation of the secular variation.** Here we separately analyse the couplings introduced in the coupled Earth dynamo model and their effect on the geographical localisation of the magnetic secular variation. To that end we use

model G, which introduces only the gravitational coupling between the inner core and the mantle, models GI and GM which additionally introduce thermochemical outer core couplings with the inner core or the mantle, in addition to the standard model and the coupled Earth dynamo model (Extended Data Figure 4). The latitudinal localisation of the secular variation is robustly observed in all models including gravitational coupling, regardless of the thermochemical coupling geometry and strength. Comparing models GI and GM shows that the longitudinal localisation observed in the coupled Earth dynamo is mainly the product of thermochemical coupling with the inner core boundary. The secondary effect of the mantle is striking, given our overestimation of the amplitude of mantle heat flow heterogeneity. We ascribe the weak impact of the mantle to the presence of the westward gyre in the outer core, which creates an efficient barrier to the deep penetration of mantle-driven thermal anomalies on the long term. Note that such a penetration was observed previously in standard models in which the gyre was absent<sup>29</sup>.

## 2 Radon transform analysis of time-longitude plots

Here we perform a Radon transform analysis of the signal represented in Figure 3, in order to extract quantitative properties concerning the azimuthally moving equatorial magnetic field. This type of analysis was previously proposed in a study of historical geomagnetic field evolution (ref. <sup>4</sup>). Full details of the methodology may be found in ref. <sup>30</sup> but briefly it involves the following steps: (i) Construct a time-longitude plot of the field at the latitude of interest, (ii) Remove the mean value from this plot i.e. subtract the time-averaged axisymmetric field, (iii) High-pass filter in time to remove low frequency trend signals longer than the record length, (iv) Perform a Radon transform: this sums the square of the field values at different slopes in the time-longitude plot, (v) Map the power vs slope distribution to a power vs azimuthal speed distribution, (vi) Repeat for all latitudes of interest. Finally one obtains a plot of power as a function of latitude and azimuthal speed such as those shown in Extended Data Figure 5. Red colours indicate a strong signal i.e. high amplitude flux features coherently traveling at a certain azimuthal speed.

Analysis of the historical field model *gufm1* using this Radon transform-based method identifies a prominent peak at low latitudes with speed of about  $-17$  km/yr. This is the signature of strong equatorial flux spots consistently moving westwards under the Atlantic hemisphere. Similar analysis of the time-longitude plot in Figure 3 from the coupled Earth dynamo model also shows a clear maximum of coherently moving power at low latitudes, in this case with speed  $-14$  km/yr. This analysis quantitatively illustrates that the coupled Earth dynamo model succeeds in localizing westward drift at low latitudes. The same analysis repeated for the standard dynamo model shows little coherent azimuthally moving power at low latitudes (see the colour scale change between Extended Data Figure 5b and 5c). The peak of coherently moving power is reached at  $+8$  km/yr eastwards in the standard model. Note however that this signal represents a small part of the total equatorial magnetic energy, which is dominated by almost stationary features that are removed as part of the processing for the Radon-transform analysis.

1. Christensen, U. R., Aubert, J. & Hulot, G. Conditions for Earth-like geodynamo models. *Earth. Plan. Sci. Lett.* **296**, 487–496 (2010).
2. Secco, R. A. & Shloessin, H. H. The electrical resistivity of solid and liquid Fe at pressures up to 7 GPa. *J. Geophys. Res.* **94**, 5887–5894 (1989).
3. Pozzo, M., Davies, C. J., Gubbins, D. & Alfè, D. Thermal and electrical conductivity of iron at Earth's core conditions. *Nature* **485**, 355–358 (2012).
4. Finlay, C. C. & Jackson, A. Equatorially dominated magnetic field change at the surface of Earth's core. *Science* **300**, 2084–2086 (2003).
5. Soderlund, K. M., King, E. M. & Aurnou, J. M. The influence of magnetic fields in planetary dynamo models. *Earth. Plan. Sci. Lett.* **333**, 9–20 (2012).
6. Aubert, J., Labrosse, S. & Poitou, C. Modelling the palaeo-evolution of the geodynamo. *Geophys. J. Int.* **179**, 1414–1428 (2009).
7. Gillet, N., Jault, D., Canet, E. & Fournier, A. Fast torsional waves and strong magnetic field within the Earth's core. *Nature* **465**, 74–77 (2010).
8. Aubert, J. Steady zonal flows in spherical shell dynamos. *J. Fluid. Mech.* **542**, 53–67 (2005).
9. Aubert, J. Flow throughout the Earth's core inverted from geomagnetic observations and numerical dynamo models. *Geophys. J. Int.* **192**, 537–556 (2013).
10. Gillet, N., Pais, M. A. & Jault, D. Ensemble inversion of time-dependent core flow models. *Geochem. Geophys. Geosystems* **10**, Q06004 (2009).
11. Christensen, U. R. & Wicht, J. Numerical dynamo simulations. In Schubert, G. (ed.) *Treatise on Geophysics. 8- Core Dynamics*, vol. 8, chap. 8 (Elsevier, Amsterdam, 2007).
12. Glatzmaier, G. A. & Roberts, P. H. Rotation and magnetism of earth's inner core. *Science* **274**, 1887–1891 (1996).
13. Buffett, B. Geodynamic estimates of the viscosity of the Earth's inner core. *Nature* **388**, 571–573 (1997).
14. Mound, J. E. & Buffett, B. A. Detection of a gravitational oscillation in length-of-day. *Earth Planet. Sci. Lett.* **243**, 383–389 (2006).
15. Aubert, J. & Dumberry, M. Steady and fluctuating inner core rotation in numerical geodynamo models. *Geophys. J. Int.* **184**, 162–170 (2011).
16. Buffett, B. A., Mound, J. E. & Jackson, A. Inversion of torsional oscillations for the structure and dynamics of Earth's core. *Geophys. J. Int.* **177**, 878–890 (2009).
17. Deguen, R. & Cardin, P. Thermochemical convection in Earth's inner core. *Geophys. J. Int.* **187**, 1101–1118 (2011).

18. Mizzon, H. & Monnereau, M. Implications of the lopsided growth for the viscosity of Earth's inner core. *Earth Planet. Sci. Lett.* **361**, 391–401 (2013).
19. Davies, C. J., Silva, L. & Mound, J. E. On the influence of a translating inner core in models of outer core convection. *Phys. Earth Planet. Inter.* **214**, 104–115 (2013).
20. Pais, M. A. & Jault, D. Quasi-geostrophic flows responsible for the secular variation of the Earth's magnetic field. *Geophys. J. Int.* **173**, 421–443 (2008).
21. Monnereau, M., Calvet, M., Margerin, L. & Souriau, A. Lopsided Growth of Earth's Inner Core. *Science* **328**, 1014–1017 (2010).
22. Alboussière, T., Deguen, R. & Melzani, M. Melting-induced stratification above the Earth's inner core due to convective translation. *Nature* **466**, 744–747 (2010).
23. Gubbins, D., Alfe, D. & Davies, C. J. Compositional instability of Earth's solid inner core. *Geophys. Res. Lett.* **40**, 1084–1088 (2013).
24. De Koker, N., Steinle-Neumann, G. & Vlcek, V. Electrical resistivity and thermal conductivity of liquid Fe alloys at high P and T, and heat flux in Earth's core. *PNAS* **109**, 4070–4073 (2012).
25. Lay, T., Hernlund, J., Garnero, E. J. & Thorne, M. S. A post-perovskite lens and D'' heat flux beneath the central pacific. *Science* **314**, 1272–1276 (2006).
26. van der Hilst, R. *et al.* Seismostratigraphy and thermal structure of Earth's core-mantle boundary region. *Science* **315**, 1813–1817 (2007).
27. Helffrich, G. & Kaneshima, S. Outer-core compositional stratification from observed core wave speed profiles. *Nature* **468**, 807–810 (2010).
28. Gubbins, D. & Davies, C. J. The stratified layer at the core-mantle boundary caused by baro-diffusion of oxygen, sulphur and silicon. *Phys. Earth. Planet. Int.* **215**, 21–28 (2013).
29. Aubert, J., Amit, H., Hulot, G. & Olson, P. Thermochemical flows couple the Earth's inner core growth to mantle heterogeneity. *Nature* **454**, 758–761 (2008).
30. Finlay, C. C. *Hydromagnetic waves in Earth's core and their influence on geomagnetic secular variation*. Ph.D. thesis, School of Earth and Environment, University of Leeds (2005).